Dirac nodal lines and induced spin Hall effect in metallic rutile oxides

Yan Sun,[1] Yang Zhang,[1,2] Chao-Xing Liu,[3] Claudia Felser,[1] and Binghai Yan[1,4,*]
[1]*Max Planck Institute for Chemical Physics of Solids, 01187 Dresden, Germany*
[2]*Leibniz Institute for Solid State and Materials Research, 01069 Dresden, Germany*
[3]*Department of Physics, the Pennsylvania State University, University Park, Pennsylvania 16802-6300, USA*
[4]*Department of Condensed Matter Physics, Weizmann Institute of Science, 7610001 Rehovot, Israel*
(Received 31 January 2017; published 2 June 2017)

We have found Dirac nodal lines (DNLs) in the band structures of metallic rutile oxides IrO_2, OsO_2, and RuO_2 and have revealed a large spin Hall conductivity contributed by these nodal lines, which explains a strong spin Hall effect (SHE) of IrO_2 discovered recently. Two types of DNLs exist. The first type forms DNL networks that extend in the whole Brillouin zone and appears only in the absence of spin-orbit coupling (SOC), which induces surface states on the boundary. Because of SOC-induced band anticrossing, a large intrinsic SHE can be realized in these compounds. The second type appears at the Brillouin zone edges and is stable against SOC because of the protection of nonsymmorphic symmetry. Besides reporting these DNL materials, our work reveals the general relationship between DNLs and the SHE, indicating a way to apply Dirac nodal materials for spintronics.

DOI: 10.1103/PhysRevB.95.235104

I. INTRODUCTION

Topological semimetals are an emerging topological phase that has attracted great attention in the condensed-matter community in recent years. Their conduction and valence bands cross each other through robust nodal points or nodal lines in the momentum space [1–3]. Distinct from normal semimetals or metals, the resultant Fermi surfaces can be characterized by nontrivial topological numbers, giving rise to exotic quantum phenomena such as Fermi arcs on the surface [1], chiral anomaly in the bulk [4,5], anomalous Hall effect (AHE) [6,7], and spin Hall effect (SHE) [8].

Dirac and Weyl semimetals are typical three-dimensional topological nodal-point semimetals, where nodal points and surface Fermi arcs have been recently discovered in real materials [9], for example, Na_3Bi [10–12], TaAs [13–17], and $MoTe_2$ [18–23]. Beyond Dirac and Weyl points, new-type symmetry-protected nodal points with three-, six- and eight-band crossings in nonsymmorphic space groups [24,25] and nodal points with triple degeneracy in symmorphic space groups [26–29] have been proposed with potential material candidates, such as MoP [26,30]. Furthermore, nodal lines ([3,31–34], and references therein) can exist in two classes of systems, according to the absence and presence of spin-orbit coupling (SOC) [33,35]. The first type without SOC has been reported in many systems (e.g., LaN, $BaSn_2$, and CaP_3) [32,36–46]. The inclusion of SOC will either gap or split the nodal lines [13,32,44–46]. The second type requires the protection of additional symmetries such as nonsymmorphic symmetries [33,47–49] and mirror reflection [31,36,50,51]. Nodal lines can cross the whole Brillouin zone (BZ) in a line shape, form closed rings inside the BZ, or form a chain containing connected rings [49]. The topological nature of a nodal line can be characterized by a quantized Berry phase π along a Wilson loop enclosing the nodal line [3,41,52–54]. On the surface, nodal-line materials were predicted to host drumheadlike surface states [36]. The theoretical search for exotic nodal phases and corresponding materials launches a race for discovering novel topological states in experiments.

Since topological nodal semimetals or metals commonly exhibit nontrivial Berry phases and strong SOC, they are expected to reveal a strong SHE as an intrinsic effect from the band structure [8]. The intrinsic SHE, in which the charge current generates the transverse spin current, is intimately related to the Berry phase and SOC [55]. Four of us recently found that the first type of Dirac nodal lines (DNLs) (without SOC) can induce a strong intrinsic SHE when turning on SOC, for example, in the TaAs-family Weyl semimetals [8]. Furthermore, it provokes us to search for topological nodal systems among known SHE (or AHE) materials. Therefore, our attention has been drawn to the SHE material IrO_2 discovered recently [56], where its thin films act as efficient spin detectors [56,57] via the inverse SHE that converts the spin current to the electric voltage. However, the microscopic understanding of the SHE is still missing for this metallic oxide. Furthermore, the strong SOC of the Ir-5*d* orbitals and nonsymmorphic symmetries of its rutile crystal structure imply that IrO_2 may host topological nodes in the band structure. Additionally, this oxide has been used for a long time for electrodes in various applications such as catalysts in water splitting ([58], and references therein) and ferroelectric memories [59].

In this paper, we have theoretically investigated the topology of the band structure of metallic rutile oxide IrO_2 and similar oxides RuO_2 and OsO_2. We observe two types of DNLs in their band structures. The first type extends the whole BZ and forms a squarelike DNL network in the absence of SOC, resulting in surface states. Joint points of the network are six- and eight-band-crossing points at the center and boundary of the BZ, respectively. These DNLs become gapped and lead to a strong SHE when SOC exists. The second type is stable against SOC and appears at the edges of the tetragonal BZ, which is protected by nonsymmorphic symmetries.

II. METHODS

To investigate the band structure and the intrinsic SHE, we have performed *ab initio* calculations based on the

*binghai.yan@weizmann.ac.il

density functional theory (DFT) with the localized atomic orbital basis and the full potential as implemented in the full-potential local-orbital (FPLO) code [60]. The exchange-correlation functionals were considered at the generalized gradient approximation (GGA) level [61]. We adopted the experimentally measured lattice structures for RO_2 (R = Ir, Os, and Ru) compounds. By projecting the Bloch states into a highly symmetric atomic orbital like Wannier functions (O-p and R-d orbitals), we constructed tight-binding Hamiltonians and computed the intrinsic spin Hall conductivity (SHC) by the linear-response Kubo formula approach in the clean limit [55,62],

$$\sigma_{ij}^{k} = e\hbar \int_{BZ} \frac{d\vec{k}}{(2\pi)^3} \sum_{n} f_{n\vec{k}} \Omega_{n,ij}^{k}(\vec{k}),$$

$$\Omega_{n,ij}^{k}(\vec{k}) = -2\mathrm{Im} \sum_{n' \neq n} \frac{\langle n\vec{k}|J_i^k|n'\vec{k}\rangle\langle n'\vec{k}|v_j|n\vec{k}\rangle}{(E_{n\vec{k}} - E_{n'\vec{k}})^2}, \quad (1)$$

where $f_{n\vec{k}}$ is the Fermi-Dirac distribution for the nth band. The spin current operator is $J_i^k = \frac{1}{2}\{v_i, s_k\}$, with the spin operator s, the velocity operator $v_i = \frac{1}{\hbar}\frac{\partial H}{\partial k_i}$, and $i,j,k = x,y,z$. $|n\vec{k}\rangle$ is the eigenvector for the Hamiltonian H at the eigenvalue $E_{n\vec{k}}$. $\Omega_{n,ij}^{k}(\vec{k})$ is referred to as the spin Berry curvature in analogy to the ordinary Berry curvature. A $500 \times 500 \times 500$ k grid in the BZ was used for the integral of the SHC. The SHC σ_{ij}^{k} refers to the spin current ($j_i^{s,k}$), which flows along the ith direction with the spin polarization along k, generated by an electric field (E_j) along the jth direction, i.e., $j_i^{s,k} = \sigma_{ij}^{k} E_j$.

III. RESULTS AND DISCUSSIONS

A. Nonsymmorphic symmetry

Three compounds RO_2 (R = Ir, Os, and Ru) share the rutile-type lattice structure with space group $P4_2/mnm$ (No. 136), as shown in Fig. 1. A primitive unit cell contains two R atoms that sit at the corner and center of the body-centered tetragonal lattice, respectively. One R atom is surrounded by six O atoms that form a distorted octahedron. For space group No. 136, we have the following generator operations:

$$E, m_z, P, n_x \equiv \{m_x|\vec{\tau}\}, n_{4z} \equiv \{c_{4z}|\vec{\tau}\},$$

where $m_{x,z}$ are mirror reflections, c_{4z} is the fourfold rotation, P is the inversion symmetry, n_x and n_{4z} represent nonsymmorphic symmetries, and $\vec{\tau} = (\frac{1}{2}, \frac{1}{2}, \frac{1}{2})$ is the translation of one-half of a body diagonal. Additionally; the time-reversal symmetry T also appears for RO_2 systems.

It is known that electronic bands are doubly degenerate (considering spin and SOC) at every k point of the BZ owing to the coexistence of P and T. Furthermore, a generic nonsymmorphic symmetry leads to new band crossings and thus higher degeneracies at the BZ boundary. Therefore, the coexistence of P, T, and nonsymmorphic symmetries guarantees fourfold or even larger degeneracies at some k points of the BZ boundary. As discussed in the following, IrO_2 exhibits a fourfold degeneracy at the BZ edge lines, $X(Y)$-M and M-A [also see Fig. 1(d)]. Consequently, one requires $4n$ electrons for filling these bands to obtain a band insulator. However, a primitive unit cell contains two IrO_2 formula units and, in total, 42 valence electrons, failing to satisfy the precondition of a band insulator in this nonsymmorphic space group [25,63]. Therefore, IrO_2 is constrained by the lattice symmetry to be a band metal in the weak-interaction case. Recently, it has been reported that IrO_2 cannot become a Mott insulator because of a large bandwidth [64,65], while several seemingly similar iridates (e.g., Sr_2IrO_4) are known as $5d$ Mott insulators with the $J_{\mathrm{eff}} = 1/2$ state [66,67].

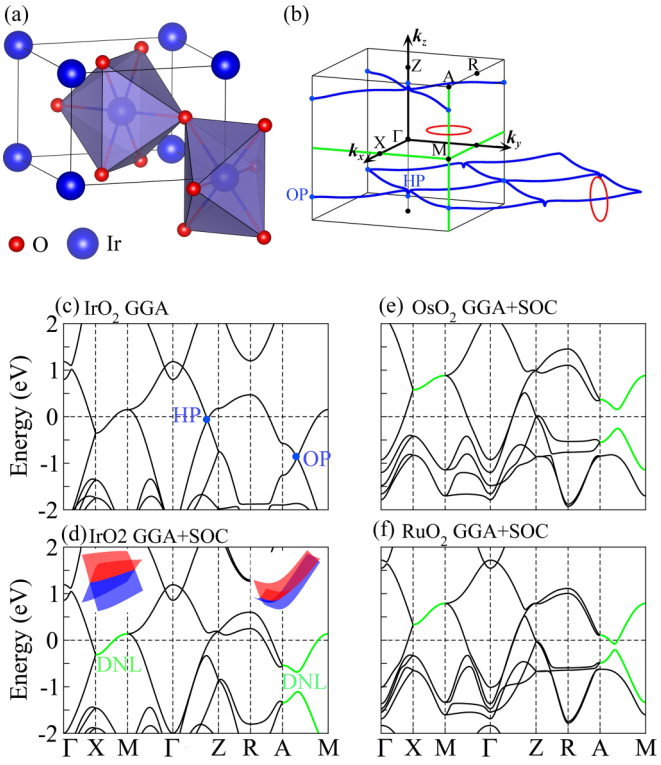

FIG. 1. (a) Rutile lattice structure of IrO_2. (b) The tetragonal BZ of IrO_2. DNLs (blue lines) without SOC form networks inside the BZ, and the corresponding Wilson loop around it (red circle) gives a π Berry phase. The connection points of the network are hexatruple points (HPs) and octuple points (OPs). The DNLs (green) with SOC are lines along X-M and M-A at the BZ boundary, and the Wilson loop around them has zero Berry phase. (c) Band structure for IrO_2 without SOC. The HP and OP are indicated by blue dots. (d)–(f) Band structures for IrO_2, OsO_2, and RuO_2 with SOC. The DNLs on X-M and M-A are highlighted by green lines. In (d), the three-dimensional (3D) band dispersion around the DNLs is shown as insets.

B. Dirac nodal lines without SOC

We first investigate the band structures without including SOC. As shown in Fig. 1(c), six-band and eight-band crossing points (including spin) appear at the Γ-Z and M-A axes, respectively, which are noted as a hexatruple point (HP) and an octuple point (OP), respectively. There is a DNL connecting neighboring HP and OP in the BZ, forming a network in the k space, as indicated by Figs. 1(b) and 3(a). Two layers of networks are present above and below the $k_z = 0$ plane, respectively, and can be transformed to each other by P or T. DNLs exist inside the (110) and ($\bar{1}$10) mirror planes and originate from the crossing of $d_{x^2-y^2}$ and $d_{xz,yz}$ bands.

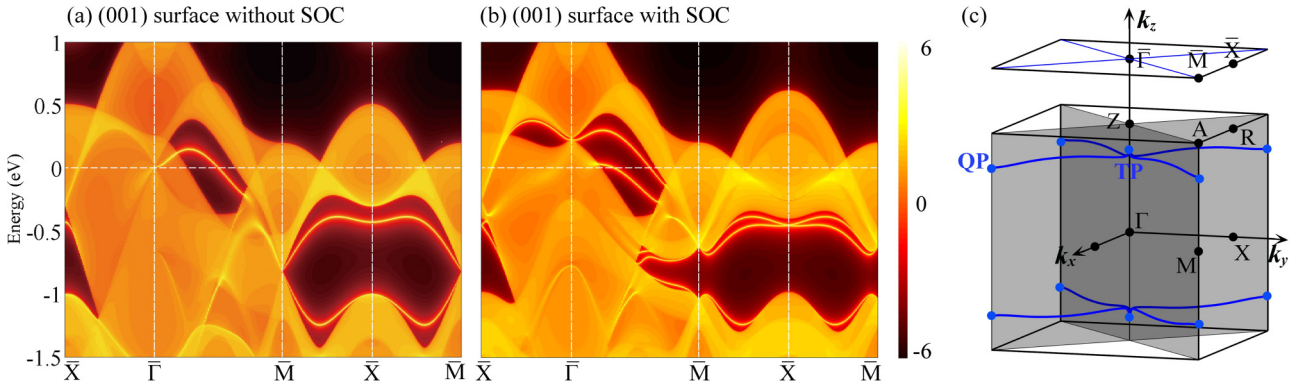

FIG. 2. Surface band structure for IrO_2 projected to the (001) surface (a) without and (b) with SOC. The brightness of color represents the weight of the surface states. (c) The projection of the bulk BZ to the surface BZ with DNLs.

Here, $d_{x^2-y^2}$ and $d_{xz,yz}$ bands are all doubly degenerate owing to P and T and exhibit opposite eigenvalues -1 and $+1$, respectively, for each mirror reflection. The mirror symmetry protects the four-band crossing in the absence of SOC.

The topology of a DNL is characterized by the nontrivial Berry phase (or winding number) along a closed path that includes the DNL. We choose a loop along which the system is fully gapped, as indicated in Fig. 1(b) [52,53]. The Berry phase for all "occupied" bands is found to be a quantized value, π. This nonzero Berry phase further leads to surface states. When projecting to the (001) surface, the nodal band structure exhibits a local energy gap between $\bar{M}$ and $\bar{X}$ in the surface BZ. Two layers of DNL networks overlap in the (001) surface projection. Thus, one can observe two sets of surface states (spin degenerated) connecting OPs between two adjacent $\bar{M}$ points inside the gap in Fig. 2(a).

When SOC is included and the SU(2) symmetry is broken, these DNLs including HPs and OPs are gapped [see Fig. 1(d)] since there is no additional symmetry protection. On the surface, original spinless surface states split into two Rashba-like spin channels [see Fig. 2(b)]. Because of the lack of robust symmetry protection (e.g., P is commonly breaking on the surface), these surface states may appear or disappear according to the surface boundary condition.

C. Dirac nodal lines with SOC

The $k_x = \pi$ and $k_y = \pi$ planes are actually Dirac nodal planes in the absence of SOC. The presence of SOC gaps these planes and only leaves DNLs along some high-symmetry lines, X-M and M-A. By taking the DNL along X-M as an example, we can understand the fourfold degeneracy by considering time-reversal symmetry T, point-group symmetries, m_z, P, and nonsymmorphic symmetry n_x. Since $[m_z, H] = 0$ in the $k_z = 0$ plane, we can choose the eigenstates of Hamiltonian H with definite mirror parity for $\vec{k}$ along X-M,

$$\begin{aligned} H(\vec{k})|\phi_\pm(\vec{k})\rangle &= E_\pm(\vec{k})|\phi_\pm(\vec{k})\rangle, \\ m_z|\phi_\pm(\vec{k})\rangle &= \pm i|\phi_\pm(\vec{k})\rangle, \end{aligned} \tag{2}$$

where i is from the spin. First, we know $[TP, m_z] = 0$. Therefore, we have

$$\begin{aligned} m_z[TP|\phi_\alpha(\vec{k})]\rangle &= TP[m_z|\phi_\alpha(\vec{k})\rangle] \\ = TP[i\alpha|\phi_\alpha(\vec{k})\rangle] &= -i\alpha[TP|\phi_\alpha(\vec{k})\rangle], \end{aligned} \tag{3}$$

where $\alpha = \pm 1$. Therefore, $TP|\phi_\alpha(\vec{k})\rangle$ is also an eigenstate at $\vec{k}(TP\vec{k} = \vec{k})$ with the mirror parity $-i\alpha$, where the $-$ sign is from the complex conjugate in T. Next, we consider the commutation between m_z and the glide mirror symmetry n_x, both of which act in real space (x,y,z) and the spin space simultaneously. In real space, we have

$$\begin{aligned} (x,y,z) &\xrightarrow{n_x} \left(-x+\tfrac{1}{2}, y+\tfrac{1}{2}, z+\tfrac{1}{2}\right) \\ &\xrightarrow{m_z} \left(-x+\tfrac{1}{2}, y+\tfrac{1}{2}, -z-\tfrac{1}{2}\right), \\ (x,y,z) &\xrightarrow{m_z} (x,y,-z) \\ &\xrightarrow{n_x} \left(-x+\tfrac{1}{2}, y+\tfrac{1}{2}, -z+\tfrac{1}{2}\right), \\ m_z n_x &= T_{(0,0,-1)} n_x m_z, \end{aligned} \tag{4}$$

where $T_{(0,0,-1)} = e^{ik_z}$ is the translation operator when acting on the Bloch wave function. In the spin space, $m_z = i\sigma_z$ and $n_x = i\sigma_x$, and thus $m_z n_x = -n_x m_z$. By combining the real space and the spin space, we obtain

$$m_z n_x = e^{ik_z}(-1) n_x m_z = -n_x m_z. \tag{5}$$

Therefore, $n_x|\phi_\alpha(\vec{k})\rangle$ is also an eigenstate at $\vec{k}(n_x\vec{k} = \vec{k})$, but with a mirror parity $-i\alpha$. Further, the combination of TPn_x leads to one more state $TPn_x|\phi_\alpha(\vec{k})\rangle$ with a mirror parity $+i\alpha$.

In total, we can have four eigenstates, $|\phi_\alpha(\vec{k})\rangle$, $TP|\phi_\alpha(\vec{k})\rangle$, $n_x|\phi_\alpha(\vec{k})\rangle$, and $TPn_x|\phi_\alpha(\vec{k})\rangle$ for $\vec{k}(\pi,k_y,0)$ along X-M. The mirror parities of m_z are $+i\alpha$ for $|\phi_\alpha(\vec{k})\rangle$ and $TPn_x|\phi_\alpha(\vec{k})\rangle$, and $-i\alpha$ for $TP|\phi_\alpha(\vec{k})\rangle$ and $n_x|\phi_\alpha(\vec{k})\rangle$. Next, we will prove that they are orthogonal to each other, i.e., two eigenstates with the same mirror parity are orthogonal, $\langle\phi_\alpha(\vec{k})|TPn_x|\phi_\alpha(\vec{k})\rangle = 0$. This requires that TPn_x is antiunitary. In real space, we have

$$\begin{aligned} (x,y,z) &\xrightarrow{Pn_x} \left(x-\tfrac{1}{2}, -y-\tfrac{1}{2}, -z-\tfrac{1}{2}\right) \\ &\xrightarrow{Pn_x} (x-1,y,z). \end{aligned} \tag{6}$$

In the spin space, $P = 1$ and $n_x = i\sigma_x$. Therefore, we have $(Pn_x)^2 = -e^{ik_x}$. Considering $T^2 = -1$ for spinful fermions, we obtain $(TPn_x)^2 = e^{ik_x} = -1$ for $\vec{k} = (\pi,k_y,0)$. Since TPn_x is an antiunitary operator that satisfies $\langle\phi|\psi\rangle =$

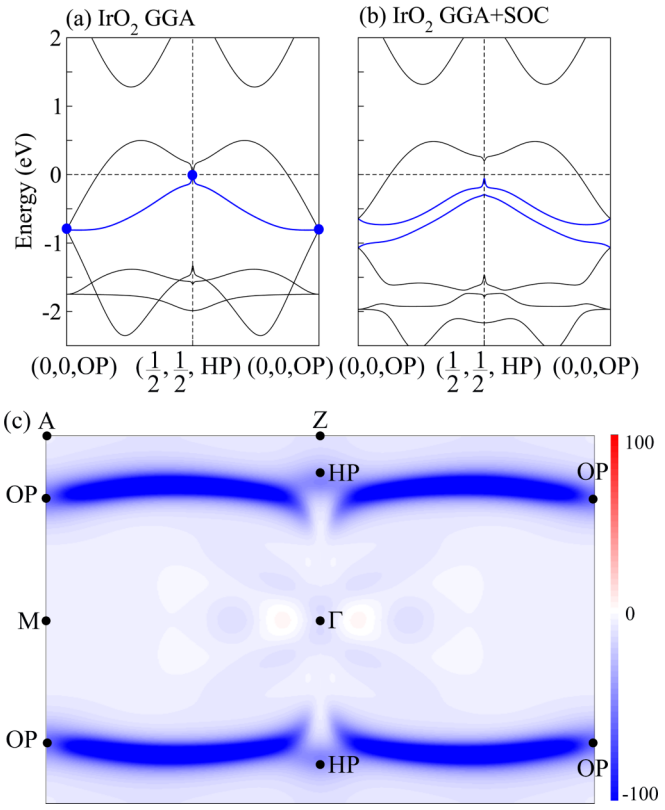

FIG. 3. DNLs and SHE in IrO_2. (a) Band structure without SOC along a first-type DNL. Blue curves represent the DNL that connects the HP and the OP in the (110) or ($\bar{1}$10) mirror plane. (b) Band structure with SOC along the same line. A gap opens along the nodal line due to SOC. (c) Distribution of the spin Berry curvature $\Omega^x_{n,yz}(\vec{k})$ inside the (110) mirror plane. Here, $\Omega^x_{n,yz}(\vec{k})$ is summarized over all bands below the SOC split gap. It is clear that the spin Berry curvature is dominantly contributed by the DNL regions. The blue and red colors represent negative and positive values of the spin Berry curvature in units of $(\text{Å}^{-1})^2$.

$\langle TPn_x\psi|TPn_x\phi\rangle$, we have

$$\begin{aligned}&\langle\phi_\alpha(\vec{k})|TPn_x|\phi_\alpha(\vec{k})\rangle\\&=\langle(TPn_x)^2\phi_\alpha(\vec{k})|TPn_x|\phi_\alpha(\vec{k})\rangle\\&=-\langle\phi_\alpha(\vec{k})|TPn_x|\phi_\alpha(\vec{k})\rangle=0,\end{aligned}\tag{7}$$

which means the states $TP|\phi_\alpha(\vec{k})\rangle$ and $n_x|\phi_\alpha(\vec{k})\rangle$ are orthogonal to each other.

Therefore, we prove that there are four degenerate orthogonal eigenstates along the X-M line. We point out that the nonsymmorphic symmetry is crucial to protect the fourfold degeneracy, while only P,T, and m_z cannot stabilize DNLs. Likewise, we can also understand the fourfold degeneracy along the M-A line considering m_z, P, T, and another nonsymmorphic symmetry n_{4z}.

These DNLs protected by nonsymmorphic symmetries are similar to those DNLs observed at the BZ edges in ZrSiS and HfSiS (e.g., [48,68]). We find that the Berry phase along a loop [indicated in Fig. 1(b)] including such a DNL is zero. Therefore, we do not expect apparent topological surface states related to these DNLs. It is still interesting to point out that the density of states scales linearly to the energy for DNLs. Then one can expect different correlation effects in DNL semimetals from a nodal-point semimetal and a normal metal [33,69]. For IrO_2, such DNLs appear at the Fermi energy, while they stay far below the Fermi energy in ZrSiS-type compounds. These DNLs may be responsible for the high conductivity and large magnetoresistance [70,71].

D. Dirac nodal lines and spin Hall effect

The first type of DNLs, i.e., DNL networks without SOC, indicate the existence of a strong SHE in RO_2. It is known that band anticrossing induced by SOC can lead to a large intrinsic SHC. To maximize the SHC, one needs to increase the number of band anticrossing points, i.e., nodal points in the absence of SOC. Therefore, a DNL, i.e., an assemble of continual nodal points in the BZ, can induce a strong SHE. The DNL networks that constitute many DNLs will further enhance the SHE. Because such type of DNLs without SOC are usually protected by the mirror symmetry, it will be insightful to look for SHE materials in space groups that host many mirror or glide mirror planes. This argument seems consistent with the fact that current best SHE materials are usually Pt and W metals (e.g., [72,73]) from the high-symmetry space groups.

Next, we compute the intrinsic SHC for RO_2 compounds following Eq. (1) based on the band structure including SOC. The SHC σ^k_{ij} is a second-order tensor with 27 elements. The number of independent nonzero elements of the SHC tensor is constrained by the symmetry of the system. We have only three independent nonzero elements, $\sigma^z_{xy}=-\sigma^z_{yx}$, $\sigma^y_{zx}=-\sigma^x_{zy}$, and $\sigma^x_{yz}=-\sigma^y_{xz}$. We list their values in Table I for all three compounds. The SHC of OsO_2 is larger than that of RuO_2, and Os-5d bands exhibit much stronger SOC than Ru-4d bands. The SHC is dependent on the Fermi energy of the system. Because Ir has one more electron than Os/Ru, the Fermi surface of IrO_2 is higher than that of OsO_2 and RuO_2, although their band structures look very similar [see Figs. 1(d)–1(f)]. Thus, IrO_2 displays a smaller SHC than OsO_2, although Ir has stronger SOC. For all three compounds, the SHC is very anisotropic, as can be seen from Table I. Here, the largest SHC of RO_2 is still smaller than that of Pt [$\sigma^z_{xy}\sim 2000(\hbar/e)(\Omega\,\text{cm})^{-1}$]. However, RO_2 may exhibit a large spin Hall angle (the ratio of the SHC over the charge conductivity) owing to their high resistivity compared to a pure metal, as already found in IrO_2 [56].

Here, we also demonstrate the direct correspondence between DNLs and the SHC. Since the SHC is obtained by integrating the spin Berry curvature over the BZ, we show the distribution of $\Omega^x_{n,yz}(\vec{k})$ in the (110) mirror plane that hosts DNLs. In the band structure along DNLs in Fig. 3,

TABLE I. SHC for IrO_2, OsO_2, and RuO_2. The Fermi energy is set to the charge neutral point. The SHC is in units of $(\hbar/e)(\Omega\,\text{cm})^{-1}$.

	IrO_2	OsO_2	RuO_2
σ^z_{xy}	8	9	83
σ^y_{zx}	–253	–311	–238
σ^x_{yz}	–161	–541	–284

the SOC clearly gaps a DNL that connects a HP and an OP. Correspondingly, one can find two "hot lines" of the spin Berry curvature, which is the anticrossing region of the DNLs. Thus, it is clear that the first-type DNLs contribute to a large SHC for IrO_2-type materials. In contrast, the second-type DNLs at the BZ edges [e.g., that along M-A in Fig. 3(c)] show a slight contribution to the SHC.

IV. CONCLUSIONS

To summarize, we found two types of DNLs in metallic rutile oxides IrO_2, OsO_2, and RuO_2. First-type DNLs form networks that extend in the whole BZ and appear only in the absence of SOC, which induces surface states at the boundary. The second type of DNLs is stable against SOC because of the protection of nonsymmorphic symmetry. Because of the SOC-induced gap for first-type DNLs, a large intrinsic SHE can be realized in these compounds. This explains the strong SHE observed in IrO_2 in the previous experiment. Moreover, our calculation suggests that OsO_2 will behave even better than IrO_2 in SHE devices, as OsO_2 shows a larger intrinsic SHC. Our work implies that first-type DNLs (or nodal points that can be gapped by SOC) and the SHE may be commonly related to each other, indicating guiding principles to search for DNLs in SHE materials or enhance the SHE by DNLs in the band structure. For example, it will be insightful to look for SHE materials in high-symmetry space groups with many mirror or glide mirror planes, which can induce the first type of DNLs.

ACKNOWLEDGMENTS

Thanks to Klaus Koepernik for the helpful discussion about Wannier function projection from FPLO code. We thank Jakub Zelezny and Lukas Müchler for fruitful discussions. This work was financially supported by the ERC (Advanced Grant No. 291472 "Idea Heusler"). Y.Z. and B.Y. acknowledge German Research Foundation (DFG), Grant No. SFB 1143.

[1] Xian Gang Wan, Ari M. Turner, Ashvin Vishwanath, and Sergey Y. Savrasov, Topological semimetal and Fermi-arc surface states in the electronic structure of pyrochlore iridates, Phys. Rev. B **83**, 205101 (2011).

[2] Grigorij E. Volovik, *The Universe in A Helium Droplet* (Clarendon, Oxford, 2003).

[3] A. A. Burkov, M. D. Hook, and Leon Balents, Topological nodal semimetals, Phys. Rev. B **84**, 235126 (2011).

[4] H. B. Nielsen and Masao Ninomiya, The Adler-Bell-Jackiw anomaly and Weyl fermions in a crystal, Phys. Lett. B **130**, 389 (1983).

[5] D. T. Son and B. Z. Spivak, Chiral anomaly and classical negative magnetoresistance of Weyl metals, Phys. Rev. B **88**, 104412 (2013).

[6] Kai-Yu Yang, Yuan-Ming Lu, and Ying Ran, Quantum Hall effects in a Weyl semimetal: Possible application in pyrochlore iridates, Phys. Rev. B **84**, 075129 (2011).

[7] A. A. Burkov, Anomalous Hall Effect in Weyl Metals, Phys. Rev. Lett. **113**, 187202 (2014).

[8] Yan Sun, Yang Zhang, Claudia Felser, and Binghai Yan, Strong Intrinsic Spin Hall Effect in the TaAs Family of Weyl Semimetals, Phys. Rev. Lett. **117**, 146403 (2016).

[9] Binghai Yan and Claudia Felser, Topological materials: Weyl semimetals, Annu. Rev. Condens. Matter Phys. **8**, 337 (2017).

[10] Zhijun Wang, Yan Sun, Xing-Qiu Chen, Cesare Franchini, Gang Xu, Hongming Weng, Xi Dai, and Zhong Fang, Dirac semimetal and topological phase transitions in A_3Bi (A= Na, K, Rb), Phys. Rev. B **85**, 195320 (2012).

[11] Z. K. Liu, B. Zhou, Y. Zhang, Z. J. Wang, H. M. Weng, D. Prabhakaran, S.-K. Mo, Z. X. Shen, Z. Fang, X. Dai, Z. Hussain, and Y. L. Chen, Discovery of a three-dimensional topological Dirac semimetal, Na_3Bi, Science **343**, 864 (2014).

[12] S.Y. Xu, C. Liu, S. K. Kushwaha, R. Sankar, J. W. Krizan, I. Belopolski, M. Neupane, G. Bian, N. Alidoust, T. R. Chang, H. T. Jeng, C. Y. Huang, W. F. Tsai, H. Lin, P. P. Shibayev, F. C. Chou, R. J. Cava, and M. Z. Hasan, Observation of Fermi arc surface states in a topological metal, Science **347**, 294 (2015).

[13] Hongming Weng, Chen Fang, Zhong Fang, B. A. Bernevig, and Xi Dai, Weyl Semimetal Phase in Noncentrosymmetric Transition-Metal Monophosphides, Phys. Rev. X **5**, 011029 (2015).

[14] Shin-Ming Huang, Su-Yang Xu, Ilya Belopolski, Chi-Cheng Lee, Guoqing Chang, BaoKai Wang, Nasser Alidoust, Guang Bian, Madhab Neupane, Chenglong Zhang, Shuang Jia, Arun Bansil, Hsin Lin, and M. Z. Hasan, A Weyl Fermion semimetal with surface Fermi arcs in the transition metal monopnictide TaAs class, Nat. Commun. **6**, 8373 (2015).

[15] B. Q. Lv, H. M. Weng, B. B. Fu, X. P. Wang, H. Miao, J. Ma, P. Richard, X. C. Huang, L. X. Zhao, G. F. Chen, Z. Fang, X. Dai, T. Qian, and H. Ding, Experimental Discovery of Weyl Semimetal TaAs, Phys. Rev. X **5**, 031013 (2015).

[16] Su-Yang Xu, Ilya Belopolski, Nasser Alidoust, Madhab Neupane, Guang Bian, Chenglong Zhang, Raman Sankar, Guoqing Chang, Yuan Zhujun, Chi-Cheng Lee, Huang Shin-Ming, Hao Zheng, Jie Ma, Daniel S. Sanchez, BaoKai Wang, Arun Bansil, Fangcheng Chou, Pavel P. Shibayev, Hsin Lin, Shuang Jia, and M. Zahid Hasan, Discovery of a Weyl fermion semimetal and topological Fermi arcs, Science **349**, 613 (2015).

[17] L. X. Yang, Z. K. Liu, Y. Sun, H. Peng, H. F. Yang, T. Zhang, B. Zhou, Y. Zhang, Y. F. Guo, M. Rahn, D. Prabhakaran, Z. Hussain, S. K. Mo, C. Felser, B. Yan, and Y. L. Chen, Weyl semimetal phase in non-centrosymmetric compound TaAs, Nat. Phys. **11**, 728 (2015).

[18] Alexey A. Soluyanov, Dominik Gresch, Zhijun Wang, Quansheng Wu, Matthias Troyer, Xi Dai, and B. Andrei Bernevig, Type-II Weyl semimetals, Nature (London) **527**, 495 (2015).

[19] Y. Sun, S.-C. Wu, M. N. Ali, C. Felser, and B. Yan, Prediction of Weyl semimetal in orthorhombic $MoTe_2$, Phys. Rev. B **92**, 161107(R) (2015).

[20] Ke Deng, Guoliang Wan, Peng Deng, Kenan Zhang, Shijie Ding, Eryin Wang, Mingzhe Yan, Huaqing Huang, Hongyun Zhang, Zhilin Xu, Jonathan Denlinger, Alexei Fedorov, Haitao Yang, Wenhui Duan, Hong Yao, Yang Wu, Shoushan Fan, Haijun Zhang, Xi Chen, and Shuyun Zhou, Experimental observation of

topological Fermi arcs in type-II Weyl semimetal $MoTe_2$, Nat. Phys. **12**, 1105 (2016).

[21] J. Jiang, Z. K. Liu, Y. Sun, H. F. Yang, C. R. Rajamathi, Y. P. Qi, L. X. Yang, C. Chen, H. Peng, C. C. Hwang, S. Z. Sun, S.-K. Mo, I. Vobornik, J. Fujii, S. S. P. Parkin, C. Felser, Binghai Yan, and Y. L. Chen, Signature of type-II Weyl semimetal phase in $MoTe_2$, Nat. Commun. **8**, 13973 (2017).

[22] Lunan Huang, Timothy M. McCormick, Masayuki Ochi, Zhiying Zhao, Michi-To Suzuki, Ryotaro Arita, Yun Wu, Daixiang Mou, Huibo Cao, Jiaqiang Yan, Nandini Trivedi, and Adam Kaminski, Spectroscopic evidence for a type II Weyl semimetallic state in $MoTe_2$, Nat. Mater. **15**, 1155 (2016).

[23] A. Tamai, Q. S. Wu, I. Cucchi, F. Y. Bruno, S. Ricco, T. K. Kim, M. Hoesch, C. Barreteau, E. Giannini, C. Besnard, A. A. Soluyanov, and F. Baumberger, Fermi Arcs and Their Topological Character in the Candidate Type-II Weyl Semimetal $MoTe_2$, Phys. Rev. X **6**, 031021 (2016).

[24] Benjamin J. Wieder, Youngkuk Kim, A. M. Rappe, and C. L. Kane, Double Dirac Semimetals in Three Dimensions, Phys. Rev. Lett. **116**, 186402 (2016).

[25] Barry Bradlyn, Jennifer Cano, Zhijun Wang, M. G. Vergniory, C. Felser, R. J. Cava, and B. Andrei Bernevig, Beyond Dirac and Weyl fermions: Unconventional quasiparticles in conventional crystals, Science **353**, 5037 (2016).

[26] Ziming Zhu, Georg W. Winkler, Quansheng Wu, Ju Li, and Alexey A. Soluyanov, Triple Point Topological Metals, Phys. Rev. X **6**, 031003 (2016).

[27] Georg W. Winkler, Quansheng Wu, Matthias Troyer, Peter Krogstrup, and Alexey A. Soluyanov, Topological Phases in $InAs_{1-x}Sb_x$: From Novel Topological Semimetal to Majorana Wire, Phys. Rev. Lett. **117**, 076403 (2016).

[28] Hongming Weng, Chen Fang, Zhong Fang, and Xi Dai, Topological semimetals with triply degenerate nodal points in θ-phase tantalum nitride, Phys. Rev. B **93**, 241202 (2016).

[29] Hongming Weng, Chen Fang, Zhong Fang, and Xi Dai, Coexistence of Weyl fermion and massless triply degenerate nodal points, Phys. Rev. B **94**, 165201 (2016).

[30] B. Q. Lv, Z. L. Feng, Q. N. Xu, J. Z. Ma, and L. Y. Kong, Experimental observation of three-component "new fermions" in topological semimetal MoP, arXiv:1610.08877.

[31] Ching-Kai Chiu and Andreas P. Schnyder, Classification of reflection-symmetry-protected topological semimetals and nodal superconductors, Phys. Rev. B **90**, 205136 (2014).

[32] Minggang Zeng, Chen Fang, Guoqing Chang, Yu-An Chen, Timothy Hsieh, Arun Bansil, Hsin Lin, and Liang Fu, Topological semimetals and topological insulators in rare earth monopnictides, arXiv:1504.03492v1.

[33] Chen Fang, Yige Chen, Hae-Young Kee, and Liang Fu, Topological nodal line semimetals with and without spin-orbital coupling, Phys. Rev. B **92**, 081201(R) (2015).

[34] Ching-Kai Chiu, Jeffrey C. Y. Teo, Andreas P. Schnyder, and Shinsei Ryu, Classification of topological quantum matter with symmetries, Rev. Mod. Phys. **88**, 035005 (2016).

[35] Chen Fang, Hongming Weng, Xi Dai, and Zhong Fang, Topological nodal line semimetals, Chin. Phys. B **25**, 117106 (2016).

[36] Hongming Weng, Yunye Liang, Qiunan Xu, Rui Yu, Zhong Fang, Xi Dai, and Yoshiyuki Kawazoe, Topological node-line semimetal in three-dimensional graphene networks, Phys. Rev. B **92**, 045108 (2015).

[37] Lilia S. Xie, Leslie M. Schoop, Elizabeth M. Seibel, Quinn D. Gibson, Weiwei Xie, and Robert J. Cava, A new form of Ca_3P_2 with a ring of Dirac nodes, APL Mater. **3**, 083602 (2015).

[38] Youngkuk Kim, Benjamin J. Wieder, C. L. Kane, and Andrew M. Rappe, Dirac Line Nodes in Inversion-Symmetric Crystals, Phys. Rev. Lett. **115**, 036806 (2015).

[39] Rui Yu, Hongming Weng, Zhong Fang, Xi Dai, and Xiao Hu, Topological Node-Line Semimetal and Dirac Semimetal State in Antiperovskite Cu_3PdN, Phys. Rev. Lett. **115**, 036807 (2015).

[40] Yuanping Chen, Yuee Xie, Shengyuan A. Yang, Hui Pan, Fan Zhang, Marvin L. Cohen, and Shengbai Zhang, Nanostructured carbon allotropes with Weyl-like loops and points, Nano Lett. **15**, 6974 (2015).

[41] Y. H. Chan, Ching-Kai Chiu, M. Y. Chou, and Andreas P. Schnyder, Ca_3P_2 and other topological semimetals with line nodes and drumhead surface states, Phys. Rev. B **93**, 205132 (2016).

[42] Ronghan Li, Hui Ma, Xiyue Cheng, Shoulong Wang, Dianzhong Li, Zhengyu Zhang, Yiyi Li, and Xing-Qiu Chen, Dirac Node Lines in Pure Alkali Earth Metals, Phys. Rev. Lett. **117**, 096401 (2016).

[43] Motoaki Hirayama, Ryo Okugawa, Takashi Miyake, and Shuichi Murakami, Topological Dirac nodal lines in fcc calcium, strontium, and ytterbium, Nat. Commun. **8**, 14022 (2017).

[44] Huaqing Huang, Jianpeng Liu, David Vanderbilt, and Wenhui Duan, Topological nodal-line semimetals in alkaline-earth stannides, germanides, and silicide, Phys. Rev. B **93**, 201114(R) (2016).

[45] Steve M. Young, S. Manni, Junping Shao, Paul C. Canfield, and Aleksey N. Kolmogorov, $BaSn_2$: A wide-gap strong topological insulator, Phys. Rev. B **95**, 085116 (2017).

[46] Qiunan Xu, Rui Yu, Zhong Fang, Xi Dai, and Hongming Weng, Topological nodal line semimetals in the CaP_3 family of materials, Phys. Rev. B **95**, 045136 (2017).

[47] Steve M. Young and Charles L. Kane, Dirac Semimetals in Two Dimensions, Phys. Rev. Lett. **115**, 126803 (2015).

[48] Leslie M. Schoop, Mazhar N. Ali, Carola Straßer, Andreas Topp, Andrei Varykhalov, Dmitry Marchenko, Viola Duppel, Stuart S. P. Parkin, Bettina V. Lotsch, and Christian R. Ast, Dirac cone protected by non-symmorphic symmetry and three-dimensional Dirac line node in ZrSiS, Nat. Commun. **7**, 11696 (2016).

[49] Tomáš Bzdušek, Quansheng Wu, Andreas Rüegg, Manfred Sigrist, and Alexey A. Soluyanov, Nodal-chain metals, Nature (London) **538**, 75 (2016).

[50] Mazhar N. Ali, Quinn D. Gibson, T. Klimczuk, and R. J. Cava, Noncentrosymmetric superconductor with a bulk three-dimensional Dirac cone gapped by strong spin-orbit coupling, Phys. Rev. B **89**, 020505 (2014).

[51] Guang Bian, Tay-Rong Chang, Raman Sankar, Su-Yang Xu, Hao Zheng, Titus Neupert, Ching-Kai Chiu, Shin-Ming Huang, Guoqing Chang, Ilya Belopolski, Daniel S. Sanchez, Madhab Neupane, Nasser Alidoust, Chang Liu, BaoKai Wang, Chi-Cheng Lee, Horng-Tay Jeng, Chenglong Zhang, Zhujun Yuan, Shuang Jia, Arun Bansil, Fangcheng Chou, Hsin Lin, and M. Zahid Hasan, Topological nodal-line fermions in spin-orbit metal $PbTaSe_2$, Nat. Commun. **7**, 10556 (2016).

[52] Rui Yu, Xiao Liang Qi, Andrei Bernevig, Zhong Fang, and Xi Dai, Equivalent expression of $\mathbb{Z}_2$ topological invariant for band insulators using the non-Abelian Berry connection, Phys. Rev. B **84**, 075119 (2011).

[53] Alexey A. Soluyanov and David Vanderbilt, Computing topological invariants without inversion symmetry, Phys. Rev. B **83**, 235401 (2011).

[54] Chen Fang, Matthew J. Gilbert, and B. A. Bernevig, Bulk topological invariants in noninteracting point group symmetric insulators, Phys. Rev. B **86**, 115112 (2012).

[55] Jairo Sinova, Sergio O. Valenzuela, J. Wunderlich, C. H. Back, and T. Jungwirth, Spin Hall effects, Rev. Mod. Phys. **87**, 1213 (2015).

[56] Kohei Fujiwara, Yasuhiro Fukuma, Jobu Matsuno, Hiroshi Idzuchi, Yasuhiro Niimi, YoshiChika Otani, and Hidenori Takagi, 5d iridium oxide as a material for spin-current detection, Nat. Commun. **4**, 2893 (2013).

[57] Zhiyong Qiu, Dazhi Hou, Takashi Kikkawa, Ken-ichi Uchida, and Eiji Saitoh, All-oxide spin Seebeck effects, Appl. Phys. Express **8**, 083001 (2015).

[58] S. David Tilley, Maurin Cornuz, Kevin Sivula, and Michael Grätzel, Light-induced water splitting with hematite: Improved nanostructure and iridium oxide catalysis, Angew. Chem. **122**, 6549 (2010).

[59] James F. Scott, *Ferroelectric Memories* (Springer-Verlag, Berlin, 2000).

[60] Klaus Koepernik and Helmut Eschrig, Full-potential nonorthogonal local-orbital minimum-basis band-structure scheme, Phys. Rev. B **59**, 1743 (1999).

[61] John P. Perdew, Kieron Burke, and Matthias Ernzerhof, Generalized Gradient Approximation Made Simple, Phys. Rev. Lett. **77**, 3865 (1996).

[62] Di Xiao, Ming-Che Chang, and Qian Niu, Berry phase effects on electronic properties, Rev. Mod. Phys. **82**, 1959 (2010).

[63] Siddharth A. Parameswaran, Ari M. Turner, Daniel P. Arovas, and Ashvin Vishwanath, Topological order and absence of band insulators at integer filling in non-symmorphic crystals, Nat. Phys. **9**, 299 (2013).

[64] J. M. Kahk, C. G. Poll, F. E. Oropeza, J. M. Ablett, D. Céolin, J.-P. Rueff, S. Agrestini, Y. Utsumi, K. D. Tsuei, Y. F. Liao, F. Borgatti, G. Panaccione, A. Regoutz, R. G. Egdell, B. J. Morgan, D. O. Scanlon, and D. J. Payne, Understanding the Electronic Structure of IrO_2 Using Hard-x-ray Photoelectron Spectroscopy and Density-Functional Theory, Phys. Rev. Lett. **112**, 117601 (2014).

[65] Woo Jin Kim, So Yeun Kim, Choong H. Kim, Chang Hee Sohn, O. B. Korneta, Seung Chul Chae, and Tae Won Noh, Spin-orbit coupling induced band structure change and orbital character of epitaxial IrO_2 films, Phys. Rev. B **93**, 045104 (2016).

[66] B. J. Kim, Hosub Jin, S. J. Moon, J.-Y. Kim, B.-G. Park, C. S. Leem, Jaejun Yu, T. W. Noh, C. Kim, S. J. Oh, J. H. Park, V. Durairaj, G. Cao, and E. Rotenberg, Novel $J_{\rm eff} = 1/2$ Mott State Induced by Relativistic Spin-Orbit Coupling in Sr_2IrO_4, Phys. Rev. Lett. **101**, 076402 (2008).

[67] B. J. Kim, H. Ohsumi, T. Komesu, S. Sakai, T. Morita, H. Takagi, and T. Arima, Phase-sensitive observation of a spin-orbital Mott state in Sr_2IrO_4, Science **323**, 1329 (2009).

[68] C. Chen, X. Xu, J. Jiang, S. C. Wu, Y. P. Qi, L. X. Yang, M. X. Wang, Y. Sun, N. B. M. Schröter, H. F. Yang, L. M. Schoop, Y. Y. Lv, J. Zhou, Y. B. Chen, S. H. Yao, M. H. Lu, Y. F. Chen, C. Felser, Binghai Yan, Z. K. Liu, and Y. L. Chen, Dirac line-nodes and effect of spin-orbit coupling in non-symmorphic critical semimetal MSiS (M=Hf, Zr), Phys. Rev. B **95**, 125126 (2017).

[69] Yejin Huh, Eun-Gook Moon, and Yong Baek Kim, Long-range Coulomb interaction in nodal-ring semimetals, Phys. Rev. B **93**, 035138 (2016).

[70] J. J. Lin, S. M. Huang, Y. H. Lin, T. C. Lee, H. Liu, X. X. Zhang, R. S. Chen, and Y. S. Huang, Low temperature electrical transport properties of RuO_2 and IrO_2 single crystals, J. Phys.: Condens. Matter **16**, 8035 (2004).

[71] W. D. Ryden, W. A. Reed, and E. S. Greiner, High-field magnetoresistance of IrO_2, Phys. Rev. B **6**, 2089 (1972).

[72] T. Tanaka, H. Kontani, M. Naito, T. Naito, D. S. Hirashima, K. Yamada, and J. Inoue, Intrinsic spin Hall effect and orbital Hall effect in 4*d* and 5*d* transition metals, Phys. Rev. B **77**, 165117 (2008).

[73] G. Y. Guo, S. Murakami, T.-W. Chen, and N. Nagaosa, Intrinsic Spin Hall Effect in Platinum: First-Principles Calculations, Phys. Rev. Lett. **100**, 096401 (2008).